This item is the archived peer-reviewed author-version of:

CFD- and radiation field modeling of a gas phase photocatalytic multi-tube reactor

CFD- and radiation field modeling of a gas phase photocatalytic multi-tube reactor

Jelle Roegiers [†‡], Jeroen van Walsem [†‡], Siegfried Denys[†,]*

† Sustainable Energy, Air & Water Technology, Department of Bioscience Engineering,

University of Antwerp, Groenenborgerlaan 171, B-2020 Antwerp, Belgium.

* E-mail: Siegfried.Denys@uantwerp.be

Fax: +32 3 265 32 25. Tel: +32 3 265 32 30.

‡ These authors contributed equally.

Keywords

Gas phase photocatalysis; multi-tube reactor; CFD; radiation field model; indoor air pollution; kinetic modeling; climate chamber

Highlights

- Development of a Multiphysics model for gas phase photocatalysis in a multi-tube reactor.

- A radiation field model for irradiance distribution was coupled with reaction kinetics.

- Optimization of all photocatalytic related parameters with CFD, based on transient FTIR measurements.

- Successful validation of the Multiphysics model for different experimental operating conditions in an airtight climate chamber.

Abstract

This paper focusses on the development of a Multiphysics model as a tool for assessing the performance of a multi-tube photoreactor. The model predicts the transient behavior of acetaldehyde concentration, as a model compound for the organic fraction of the indoor air pollutants, under varying sets of conditions. A 3D-model couples radiation field modeling with reaction kinetics and fluid dynamics in order to simulate the transport of the pollutant as it progresses through the reactor. A model-based approach is proposed to determine the layer thickness and refractive index of different P25-powder modified sol-gel coatings, using an optimization procedure to estimate these parameters based on UV-irradiance measurements. The radiation field model was able to accurately predict the irradiance on the catalytic surface within the reactor. Consequently, the radiation field model was used to define an irradiance dependent reaction rate constant in a coupled Multiphysics model. An optimization routine was deployed to estimate the adsorption, desorption- and photocatalytic reaction rate constants on the TiO_2-surface, using experimentally determined, transient outlet concentrations of acetaldehyde. Additionally, a validation test was performed in an air-tight climate chamber at much higher flow rates, higher irradiance and realistic indoor pollutant concentrations to emphasize the reliability and accuracy of the parameters for adsorption, desorption and photocatalytic reaction. The developed model makes it possible to optimize the reactor design and scale-up for commercial applications.

1   Nomenclature

A	Surface area $[m^2]$
c	Speed of light $[m/s]$
C_{CH_3CHO}	Bulk acetaldehyde concentration $[mol/m^3]$
$C_{CH_3CHO,ads.}$	Surface acetaldehyde concentration $[mol/m^2]$
$C_{Chamber}$	Acetaldehyde concentration in climate chamber $[mol/m^3]$
D	Diffusion coefficient $[m^2/s]$
$E(\lambda)$	Bandgap at wavelength λ $[eV]$
E_g	TiO_2 Bandgap $[eV]$
I	Irradiance $[W/m^2]$
$\boldsymbol{k}$	Wave vector
k_{ads}	Adsorption rate constant $[m/s]$
k_{des}	Desorption rate constant $[mol/m^2s]$
k_{pco}	Reaction rate constant $[1/s]$
k	Imaginary part of refractive index
n	Real part of refractive index
p	Pressure $[Pa]$
$\boldsymbol{q}$	Position vector
Q	Ray power $[W]$
R_{ads}	Adsorption flux $[mol/m^2s]$
R_{des}	Desorption flux $[mol/m^2s]$
R_{pco}	Photocatalytic reaction rate $[mol/m^2s]$
$\mathbf{u}$	Velocity vector
x	Optical path length $[m]$
α	Absorption coefficient $[m^{-1}]$
Γ_s	Maximum surface coverage $[mol/m^2]$
δ	Layer thickness $[m]$
λ	Wavelength $[m]$
μ	Dynamic viscosity $[Pa \cdot s]$
μ_T	Eddy viscosity $[Pa \cdot s]$
ρ	Density $[kg/m^3]$
θ	Angle with normal of a boundary
ω	Angular frequency $[rad/s]$

2

3

4

1. Introduction

Photocatalytic oxidation (PCO) technology is nowadays considered a very efficient and sustainable technology for indoor air purification, for example, integrated in HVAC systems [1–6]. Despite intensive research efforts, only a few cases of operating PCO cleaning devices are documented and patented [1,4,7]. There is still a substantial gap to be filled between lab-scale investigation of suitable photocatalysts and applied PCO technology for effective air purification. The design of an effective photocatalytic reactor is the main issue in commercializing PCO technology [8]. Each type of photocatalytic reactor has different performance criteria, but generally it can be stated that an efficient PCO reactor should achieve complete mineralization of VOCs, high proton utilization of the photocatalyst, low pressure drop and power consumption in a relatively compact vessel [8]. Furthermore, efficient operation of a PCO reactor requires insights in mass transfer rates, i.e. convective and diffusive transport towards the catalytic surface, and the kinetics of adsorption, desorption and photocatalytic reaction, as either can be the limiting factors for complete mineralization. Finite element modeling (FEM) is a numerical method for solving complex physics and is a very attractive approach for the analysis of a PCO reactor performance through integrated simulations of fluid dynamics, irradiance distribution and kinetics of desorption, adsorption and reaction at the catalytic surface. Previous studies have shown that Computational Fluid Dynamics (CFD) simulations can accurately predict the phenomena occurring in a PCO reactor, including Langmuir-Hinshelwood kinetics, considering a uniform irradiance distribution [9–13]. Only a few studies attempted to combine radiation field modeling with a CFD-model to predict the performance of a gas phase photoreactor, mainly for flat bed reactors and monolith reactors [14–17]. However, the irradiance in a flat bed reactor covers only a small range and usually shows very low local variety of the incident photon flux. The first part of this work covers the development of a radiation field model that accurately describes the irradiance distribution in a

multi-tube photocatalytic reactor with a more complex geometry and consequently, a more irregular irradiance distribution. The radiation field model was then coupled with CFD simulations, which described the air flow through the reactor and the reaction kinetics (including the effect of irradiance), to obtain the local variation of the photocatalytic reaction rate and the kinetic parameters. Acetaldehyde was used as a model compound in this study, since it is an important indoor air pollutant and an intermediate photocatalytic product of more complex VOCs [18]. As we will show, this numerical approach was able to combine complex physics and correctly predict the outlet concentration of acetaldehyde under different sets of conditions.

2. Methodology

2.1 Multi-tube photoreactor

A photocatalytic tube reactor was assembled from a cylindrical vessel of Duran® borosilicate glass with an internal diameter of 29 mm and a length of 440 mm, with an inlet and outlet as shown in Figure 1. The vessel contained 7 smaller borosilicate glass tubes (internal and external diameter 7mm and 9mm respectively; length 200 mm) that were coated with a TiO_2-based coating and positioned centrally in the vessel. Two 25 W fluorescent UV-A lamps (Philips Lighting, Belgium) with a peak wavelength at 365 nm, were positioned parallel to the reactor housing at opposite sides. Before assembling the reactor, the smaller glass tubes were dip-coated using the P25-powder modified sol-gel method. A 0.5 M titanium isopropoxide (TTIP, >98%, Agro organics) in isopropanol (I-PrOH, >98%, VWR chemicals) was prepared, diethanolamine (DEA, 99% Roth, DEA/TTIP molar ratio of 4) and water (H_2O/TTIP molar ratio of 2) were added while stirring. P25 TiO_2 was added to finalize the sol-gel and ultrasonically stirred. The glass tubes were coated with a withdrawal speed of 120 mm/min. The tubes were then air dried for 24 hours and afterwards calcined at 500°C for 1h. For more
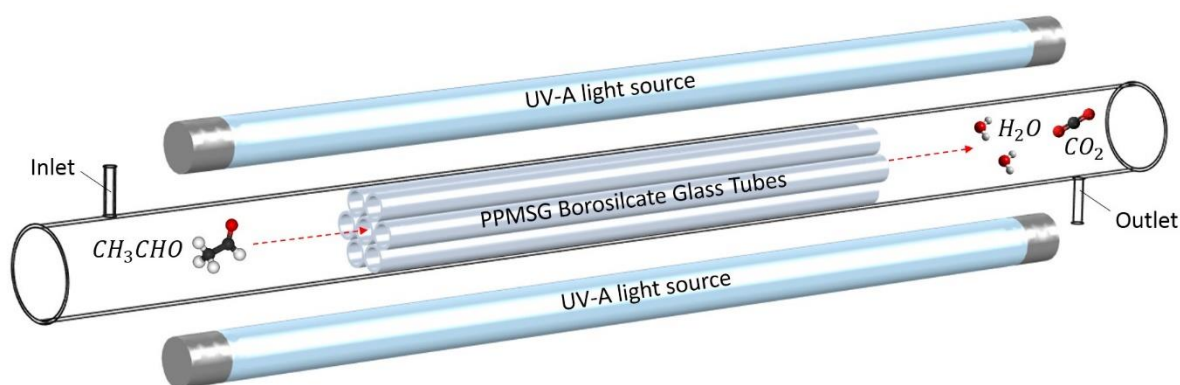

Figure 1: Schematic representation of the multi-tube photoreactor with two 25W UV-A lamps.

1 details of the preparation method, the reader is referred to van Walsem *et al.* (submitted in CES).

2 In our former work (van Walsem *et al.*, submitted in CES), coatings with 10, 30 and 50 g/L P25

3 showed the highest photocatalytic activity in the multi-tube photoreactor at relatively high flow

4 rates. Hence, these coatings were used here to develop and validate the Multiphysics model.

5 **2.2 Optical measurements**

6 The irradiance and emission spectrum were measured perpendicular to the light beam, using an

7 Avantes Avaspec-3648 spectrometer (sensor surface area of 12.5 mm²), at different positions

8 within the reactor, as shown in Figure 2 and this was done for all P25 loaded sol-gel coatings.

9 In order to calibrate and validate the radiation field model, additional irradiance measurements

10 were conducted, in which one UV-A lamp was positioned parallel to the reactor housing at a

11 distance that varied from 0.5 to 30mm during the experiment. The irradiance was measured at

12 the different positions for the 10 g/L P25-coating. The data generated from the irradiance

13 measurements on the respective positions was later used to parameterize and validate the

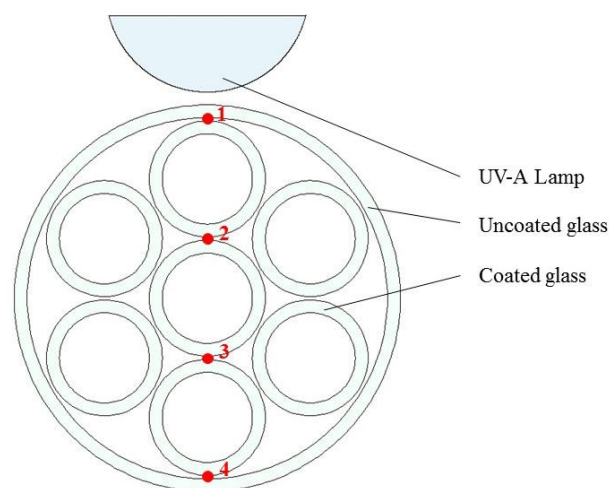14 radiation field model for 10, 30 and 50 g/L P25-coatings.

Figure 2: Positions of irradiance measurements within the multi-tube photoreactor with one 25W UV-A lamp, using an Avantes Avaspec-3648 spectrometer.

15

2.3 Photocatalytic experiments

The photocatalytic performance of the multi-tube photoreactor was investigated using acetaldehyde (Messer, 1% in N_2) as a model compound for indoor air pollution [13,18–20]. At the reactor inlet, the acetaldehyde concentration was carefully controlled by mass flow controllers and fed to the multi-tube photoreactor at a total gas flow rate of 500 cm³/min. FTIR spectroscopy measurements allowed online monitoring of the acetaldehyde concentration at the reactor outlet, based on the IR peak height at 2728 cm⁻¹, which corresponds to the ν(C-H) stretch vibration [21]. Photocatalytic experiments were conducted with two 25 W UV-A lamps at a parallel distance of 25 mm from the reactor (could not be placed closer due to practical limitations) for all P25 sol-gel coatings. In order to parametrize the parameters that describe the photocatalytic process in the reactor, experimental data was assembled by varying the inlet concentrations of acetaldehyde between 1.41 ± 0.14 and 5.92 ± 0.40 mmol/m³ (34 and 143 ppmv). Experiments were performed in three subsequent phases: The mixed gas flow first bypasses the reactor at a flow rate of 500 cm³/min and flows straight to the FTIR detector cell, in order to determine the exact inlet concentration. After 10 min of steady-state bypass, the gas flow was switched to the reactor and simultaneously the light emission source was activated. During this phase, both adsorption/desorption as well as photocatalytic reaction occurred simultaneously. 50 minutes was sufficient time to reach equilibrium outlet concentrations for all given inlet concentrations of acetaldehyde. Finally, the catalytic surface was irradiated and an artificial clean air flow at a rate of 2000 cm³/min was applied for 60 min, removing the remaining adsorbed fraction of organic compounds. The CO_2-concentration was carefully monitored during this last phase, to assure that the concentration level dropped to zero. At this point, the catalytic surface was assumed to be clean and the experiment was repeated with a higher inlet concentration.

Once the set of parameters was finalized, an ultimate validation test was performed under realistic HVAC operating conditions (high flow rates and low concentrations) in an airtight climate chamber with the same continuous photoreactor. In contrast to the FTIR set-up, where the flow rate was fixed by a mass flow controller, the flow rate in the climate chamber is now controlled by a fan, attached at the end of the reactor housing . The fan is characterized by a static pressure of 50 Pa and a free delivery flow rate of 1.085 dm³/s. Two additional fans were mounted at the climate chamber ceiling to mix the air in the chamber as well as possible. The light source consisted of two 25W UV-A lamps at a parallel distance of 5 mm to the reactor housing to achieve higher irradiance at the catalytic surface compared to the FTIR set-up. The experiments were carried out with an initial acetaldehyde concentration of 0.208 mmol/m³ (5 ppmv). The time lapse of the acetaldehyde concentration was eventually used to validate the set of intrinsic parameters under different operating conditions.

2.5 Multiphysics Modeling

2.5.1 Model geometry

The commercial software package Comsol Multiphysics v5.3 was used for finite element modeling of the air flow, acetaldehyde transport and optics. The reactor set-up, was implemented in the geometry section, for both FTIR and climate chamber experiments, including the lamps. Since the set-up is symmetrical, only halve the geometry was considered, drastically reducing the simulation time. A mesh was created for both the fluid domain as well as the glass parts, because the latter is necessary for radiation field modeling. The design of the reactor and the fact that the gas flow is parallel to the glass tubes, allowed the use of prism elements in a main part of the geometry, reducing the number of mesh elements (Figure 3). When simulating the mass transfer of acetaldehyde, a large local gradient between bulk concentrations and concentrations close to the catalytic surface was expected. Hence, an extra fine mesh was built for the fluid domain in these regions, i.e. the catalytic surface. The

remaining domains were meshed with tetrahedral elements. For the radiation field model, rays

were released from the mesh cells of the lamps and therefore the cylindrical emission source

could simply be represented by a curved surface with a mapped mesh, i.e. rectangular boundary

elements. The larger the number of elements on the emission source, the more rays that can be

released, hence a more realistic result. The complete meshed geometry consisted of 459,000

elements with an average mesh quality (skewness) of 0.70 for the FTIR set-up and 2,876,000

elements with an average mesh quality of 0.723 for the climate chamber set-up. The latter has

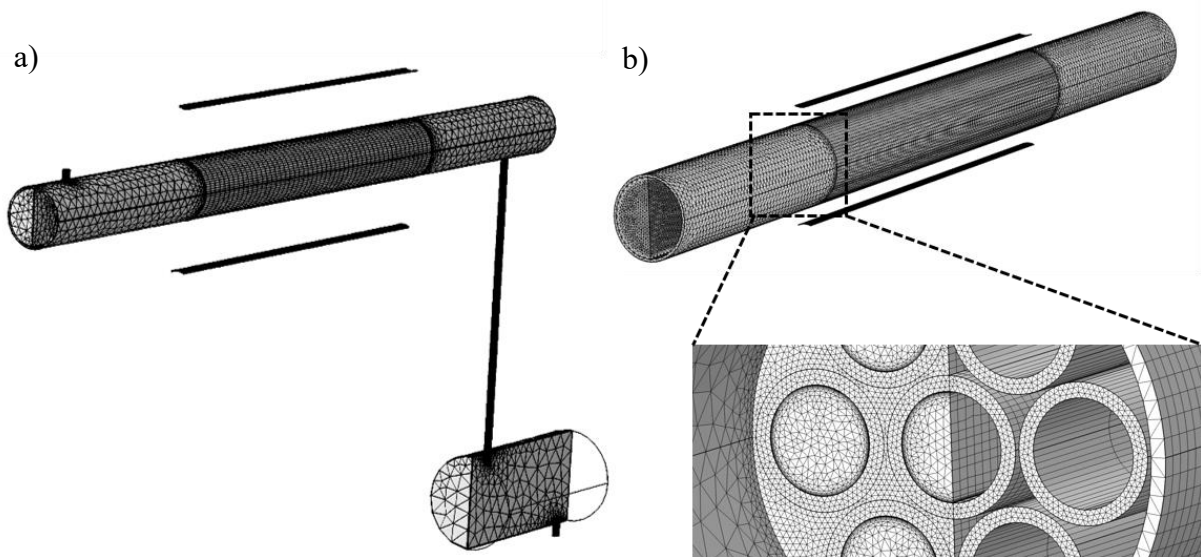a more detailed mesh due to the presence of a turbulent flow.

Figure 3 Mesh for a) FTIR set-up and b) climate chamber set-up

2.5.2 Radiation field Modeling

The incident irradiation on the catalytic surface is one of the critical factors that determine the

rate of conversion. Comsol Multiphysics v5.3.a provides an interface to model electromagnetic

wave propagation in systems in which the wavelength is several orders of magnitude smaller

than the smallest geometrical detail in the object of interest (Ray Optics - Geometrical Optics).

Light is discretized into rays that can propagate through the system. The ray trajectory is not

resolved with a finite element mesh, unless it interacts with a boundary where refraction,

reflection or absorption occurs. This way, the computational effort is reduced significantly over long travel distances compared to methods such as Monte-Carlo, discrete ordinate or Finite Volume simulations of the radiative transfer equation (RTE), which is a convenient method for optical simulations in heterogeneous photocatalytic reactors [14,22–25]. The rays were released from the mesh of the curved boundaries, which represent the lamps, with a total of 160,000 rays/lamp. An initial irradiance of 120 W/m² was measured on the surface of the UV-lamp, by integrating the spectrum over a range of 300 to 400 nm wavelength. The initial power (W) of each ray is calculated by dividing the initial ray intensity by the ray density (number of rays released per m²). The ray trajectory can be computed by solving coupled first-order differential equations [26]:

$$\begin{cases} \dfrac{d\boldsymbol{k}}{dt} = -\dfrac{\partial \omega}{\partial \boldsymbol{q}} \\ \dfrac{d\boldsymbol{q}}{dt} = \dfrac{\partial \omega}{\partial \boldsymbol{k}} \\ \omega = \dfrac{c|\boldsymbol{k}|}{n(\boldsymbol{q})} \end{cases} \qquad 1$$

with $\boldsymbol{k}$ the wave vector, ω the angular frequency, c the speed of light in vacuum, n the real part of the refractive index and $\boldsymbol{q}$ the position vector. The set of equations was solved in the time domain by a GMRES iterative solver with maximum time steps of 2 ps. The irradiance computation is based on calculations that treat each ray as a propagating wavefront, which subtend constant angles within the same domain. When a ray passes from one medium to another, the wave vector is reinitialized using Snell's law [26]:

$$\frac{\sin(\theta_i)}{\sin(\theta_r)} = \frac{n_2}{n_1} \qquad 2$$

Where θ_i and θ_r represent the angle measured from the normal of the boundary for the incident ray and the refracted ray respectively and n is the real part of the refractive index of the

respective medium. The refractive index of the borosilicate glass parts of the reactor and the external domain (domain without geometry or mesh) were 1.473 and 1 respectively. First the angle of incidence θ_i is computed, based on the dot product of the unit vector in the direction of the incident ray $\boldsymbol{n_i}$ and the unit vector $\boldsymbol{n_s}$ normal to the incident boundary [26]:

$$\theta_i = \mathrm{acos}\left(\frac{\boldsymbol{n_i} \cdot \boldsymbol{n_s}}{|\boldsymbol{n_i}||\boldsymbol{n_s}|}\right) \qquad 3$$

The direction of the refracted ray is then given by solving the following set of equations [26]:

$$\begin{cases} \boldsymbol{n_r} = \eta \boldsymbol{n_i} + \gamma \boldsymbol{n_s} \\ \gamma = -\eta \cos(\theta_i) + \cos(\theta_r) \\ \eta = \dfrac{n_1}{n_2} \\ \theta_r = \mathrm{asin}(\eta \sin(\theta_i)) \end{cases} \qquad 4$$

With $\boldsymbol{n_r}$ a unit vector in the direction of the refracted ray and θ_r the angle with the boundary normal. The power of the refracted rays is calculated with the use of the (modified) Fresnel equations at boundaries [26]. Computation of secondary rays due to reflection, was neglected to speed up the simulation. The sol-gel coating on the glass tubes was defined as a single-layer thin dielectric film with a specified film thickness and refractive index. Attenuation of the ray intensity or power due to interaction with the coating, was realized by defining an imaginary part of the refractive index k of the thin dielectric film, which is related to the absorption coefficient α from the Beer-Lambert law as:

$$\alpha = \frac{4\pi k}{\lambda_0} \qquad 5$$

With λ_0 the vacuum wave length of 365 nm, as this is the peak wavelength emitted by the UV-A lamps. Unfortunately, only limited and contradictive information is available regarding the refractive index of sol-gel coated glass substrates. Wang *et al.* proposes an empirical relation for the complex refractive index of a sol-gel coating, based on the Cauchy formula for dielectric films in a range of wavelengths between 400 and 1000 nm [27]. For the simplicity of the model,

the rays were released at the peak wavelength of the emission source, i.e. 365 nm, instead of a distribution of wavelengths. Unfortunately, the imaginary part of the refractive index k could not be extrapolated to a wavelength below 400 nm, since light absorption starts to occur at this point and therefore k would drastically increase. Chrysicopoulou *et al*. used the physical model of Forouhi–Bloomer to empirically determine the optical properties of very thin (<100 nm) sol–gel TiO_2 films in a much broader range of 200-2500 nm [28]. An irradiance-weighted expression for the imaginary part of the refractive index k_{mean} was proposed, using the Forouhi–Bloomer physical model and the emitted spectrum of the UV-A lamp, as measured by the Avantes Avaspec-3648 spectrometer :

$$k_{mean}(\lambda) = \frac{\int I(\lambda) \left[\frac{A(E(\lambda) - E_g)^2}{E(\lambda)^2 - BE(\lambda) + C} \right] d\lambda}{\int I(\lambda) \, d\lambda} \qquad 6$$

With $I(\lambda)$ the irradiance at wavelength λ retrieved from the emission spectrum of the UV-A lamp, $E(\lambda)$ the bandgap at wavelength λ, $E_g = 3.2723$ corresponding to the bandgap of TiO_2 and A, B and C empirical parameters with values of 0.2048, 8.5494 and 18.714 respectively [28]. This resulted in a k_{mean} of 0.03. The attenuation of UV-light is dependent on the imaginary part of the refractive index k, as well as the depth of light penetration:

$$Q = Q_0 \exp(-\alpha x) \qquad 7$$

with Q_0 the incident ray power, Q the transmitted ray power, α the absorption coefficient and x the optical path length, which can be calculated from the angle of incidence θ_i and the thickness of the coating layer δ [26]. The thickness of the sol-gel coating layer on glass substrates, reported in the literature, varies from 70 nm to 3μm, using the dipcoating method with a similar withdrawal speed [17,27–32]. Previous work studied the coating layer thickness of a 10 g/L P25 sol-gel coating on stainless steel plates, resulting in a thickness around 450 ± 24 nm [33]. The limited information from the literature urged for an alternative approach to estimate the

optical parameters and layer thickness. Therefore the light irradiance was measured at different points within the reactor (Figure 2) for the 10g/L P25 coating and the experimental results were used to parameterize k and δ. A parametric sweep was performed, with $k = 0.03$ and $\delta = 450\ nm$ as initial values, ranging between 0.2 to 0.4 and 70 nm to 3μm respectively. The final parametric combination was determined by the best fit of the simulated irradiance with the experimental data at the specified positions within the reactor (see Figure 2). The optical parameters were additionally validated with experimental irradiance measurements by varying the parallel distance between reactor and lamp. The optical properties of the 30g/L and 50 g/L P25-coatings were determined in a similar approach, but the refractive index, as obtained from the 10 g/L P25 coating, was now fixed.

In order to couple the ray tracing with the other physics, information regarding the ray power and irradiance needs to be transferred from the ray variables to the underlying finite element mesh. The latter was done in a separate study step by considering the last time step of the time-dependent solution of ray tracing as a steady-state solution, since the ray power remains constant, once every ray has reached beyond the reactor geometry. The power of each ray, interacting with the boundaries of interest, was accumulated and subsequently divided by the surface of the mesh cell to obtain the irradiance in W/m² as [26]:

$$I = \frac{1}{A} \sum_{i=1}^{N} Q_i \qquad \qquad 8$$

with I the local irradiance in W/m², A the surface area of the local mesh element in m², Q_i the power in W of ray i at the last time step, N the total number of rays that have interacted with the mesh element. The combination of all accumulated values provided the steady-state irradiance distribution within the reactor.

1 2.5.3 Air flow modeling & acetaldehyde transport

2 A laminar and a k-ε-turbulent incompressible air flow model were deployed for the FTIR- and

3 climate chamber set-up respectively. In contrast to the laminar flow model, the k-ε-model solves

4 for extra variables: the turbulence kinetic energy k and the rate of dissipation of turbulence

5 kinetic energy ε [34]. For the FTIR-experiments a volumetric flow rate was specified at the

6 inlet, corresponding to the experimental flow rate of 500 cm³/min and constant atmospheric

7 pressure was defined at the outlet. For the reactor in the climate chamber, the inlet boundary

8 conditions were defined by the fan characteristics, i.e. a static pressure of 50 Pa and free delivery

9 flow rate of 1.085 dm³/s. A steady-state solution was generated with a direct stationary solver ,

10 by solving the governing equations of momentum and mass continuity [34]:

$$\rho(\mathbf{u} \cdot \nabla)\mathbf{u} = \nabla \cdot \left(-p\mathbf{I} + (\mu + \mu_T)(\nabla\mathbf{u} + (\nabla\mathbf{u})^T)\right) \qquad 9$$

$$\rho\nabla(\mathbf{u}) = 0 \qquad 10$$

11 With ρ the air density (1.2044 kg/m³), $\mathbf{u}$ the velocity vector (m/s), $\mathbf{I}$ an identity matrix, p the

12 pressure (Pa), μ the dynamic viscosity (Pa·s) and μ_T the eddy viscosity (Pa·s), which is

13 calculated by the k-ε-model for a turbulent flow [34] and equals zero in the case of a laminar

14 flow. A no slip condition was applied at the reactor walls. The concentration of acetaldehyde in

15 the bulk phase was solved with the convection-diffusion equation, by coupling the velocity field

16 of the previous stationary study [34]:

$$\nabla \cdot \left(-D\nabla C_{CH_3CHO}\right) + \mathbf{u} \cdot \nabla C_{CH_3CHO} = 0 \qquad 11$$

17 With D the diffusion coefficient of acetaldehyde in air (1.25e-5 m²/s), C_{CH_3CHO} the bulk

18 concentration of acetaldehyde (mol/m³) and $\mathbf{u}$ the velocity field vector (m/s). One of the key

19 mechanisms in photocatalysis, is adsorption of organic pollutants on the TiO$_2$-catalyst surface.

20 Consequently, the adsorbed molecules are demineralized if the catalyst is activated by UV-light.

21 In order to model simultaneous adsorption/desorption and reaction at the surface, a new species

$CH_3CHO_{ads.}$ was introduced, with a corresponding surface concentration $C_{CH_3CHO,ads.}$ (mol/m²).

Adsorption/desorption was modelled as a flux from the bulk acetaldehyde towards the TiO_2-surface [11]:

$$-\boldsymbol{n} \cdot \left(-D\nabla C_{CH_3CHO}\right) = -R_{ads} + R_{des} \qquad 12$$

With **n** the normal vector of the boundary pointing towards the bulk phase. R_{ads} and R_{des} are the species fluxes towards and outwards the boundary respectively, given by the Langmuir expressions [35]:

$$R_{ads} = k_{ads} C_{CH_3CHO} \left(1 - \frac{C_{CH_3CHO,ads.}}{\Gamma_s}\right) \qquad 13$$

$$R_{des} = k_{des} \frac{C_{CH_3CHO,ads.}}{\Gamma_s} \qquad 14$$

With k_{ads} the adsorption rate constant (m/s), k_{des} the desorption rate constant (mol/m²s) and Γ_s the maximum surface coverage (mol/m²), i.e. in the case of complete saturation of all active sites on the surface. Determining the value of Γ_s was based on experimental data under dark conditions, as has been described in detail in previous work [11,13]. The change in surface concentration is based on the same rate expressions, except for the extra sink term which describes the loss of adsorbed molecules due to photocatalytic reaction [11]:

$$\frac{\partial C_{CH_3CHO,ads.}}{\partial t} = R_{ads} - R_{des} - R_{pco} \qquad 15$$

With R_{pco} the photocatalytic reaction rate (mol/m²s). The latter can be further expressed as a first order reaction rate:

$$R_{pco} = k_{pco}(I) \, C_{CH_3CHO,ads.} \qquad 16$$

Where $k_{pco}(I)$ represents the irradiance dependent photocatalytic reaction rate constant (1/s).

Several studies report the influence of irradiance on the photocatalytic reaction rate [15,17,36–38]. Often a power law relation of the reaction rate to the irradiance on the catalyst surface is observed, with a power between 0.5 and 1. Wang *et al.* observed a first order relation for irradiance up to 10 W/m² and a half order relation for higher irradiance. This expression for the photocatalytic reaction rate was opted in order to minimize the degrees of freedom in the parameter estimation. Consequently, the following equation was proposed for the reaction rate constant k_{pco}:

$$k_{pco}(I) = \begin{cases} k_0 I & , I < 10 \ W/m^2 \\ k_0\sqrt{I_0 \cdot I} & , I > 10 \ W/m^2 \end{cases} \qquad 17$$

With k_0 an empirical constant (m²/W·s) for $I < 10 \ W/m^2$, I_0 the threshold of 10 W/m² and I (W/m²) the irradiance, as derived from the radiation field model.

The validation experiment in the climate chamber was a batch operation and required an additional expression to monitor the remaining concentration acetaldehyde in the chamber. Considering perfect mixing in the climate chamber, the time change of concentration was calculated as:

$$\frac{dC_{Chamber}}{dt} = \frac{1}{V_{Chamber}}\left(\int_{A_{outlet}} (C_{CH_3CHO} v_{out})dA - \int_{A_{inlet}} (C_{Chamber} v_{in})dA \right) \qquad 18$$

With $C_{Chamber}$ the concentration of acetaldehyde in the climate chamber, A_{inlet} and A_{outlet} the surface area of the in- and outlet respectively, v_{inlet} and v_{outlet} the normal in- and outflow velocities and $V_{Chamber}$ the climate chamber volume (1.2 m³).

2.5.4 Intrinsic parameter estimation

The intrinsic reaction rate constants (k_{ads}, k_{des} and $k_{pco}(I)$) describing the key mechanisms of photocatalysis are to be determined. It should be mentioned that the parameters are not

completely intrinsic, since not all varying operating conditions are considered, such as the influence of relative humidity [39]. In our case, the intrinsic quality of the parameter refers to independence of mass transfer limitations, concentration and irradiance. The parameter estimation is based on transient acetaldehyde concentration profiles by adapting k_{ads}, k_{des} and k_0 in the Multiphysics model. This process was conducted with a derivative-free Nelder-Mead optimization algorithm to find the local minimum of a least-squares objective function [40]:

$$Objective = \sum_t \left(C_{outlet,t,exp.} - C_{outlet,t,model} \right)^2 \qquad 19$$

$C_{outlet,exp.,i}$ and $C_{outlet,model,i}$ are the outlet concentrations of the FTIR measurements and model predictions at a particular time t respectively. The data obtained from the glass tubes with 10 g/L P25 sol-gel coating were originally used for parameter optimization. The values for k_{ads} and k_{des} were determined under similar reaction conditions in previous work [11] and were taken as initial values for the optimization procedure. The 30 g/L and 50 g/L coatings essentially differ from the 10 g/L coating in adsorption capacity and layer thickness. Hence, the set of intrinsic parameters, obtained from the optimization routine, was deployed for the remaining coatings and only Γ_s and δ were altered in the Multiphysics model. Subsequently, the simulated outlet concentrations were validated against the experimental measurements for the 30 g/L and 50 g/L coatings. The validity of the parameters was further substantiated by simulating the concentration profile of acetaldehyde in the airtight climate chamber and comparing the results with the gas chromatography measurements.

3. Results and discussion

3.1 Radiation field model

The irradiance distribution inside the reactor was measured for the 10 g/L P25 sol-gel coating on positions 1 to 4 (Figure 2) for a reactor set-up with a parallel distance to the lamp of 5 mm. This data was used to parameterize the imaginary part of the refractive index layer as well as the layer of the coating. The initial values for the imaginary part of the refractive index k and layer thickness δ were 0.03 and 450 nm respectively, as these were averages based on literature values [17,27–33]. Figure 4a shows the irradiance on the different positions within the reactor, according to the radiation field model for the initial set of parameters. A parametric sweep was performed, in which the parameters k and δ varied from 0.02 to 0.04 and from 70nm to 3µm respectively. Subsequently, all parameter combinations were validated against the spectrometer measurements of the irradiance, using the coefficient of determination as criterion. Figure 4b shows the best model fit of the irradiance distribution in the reactor.
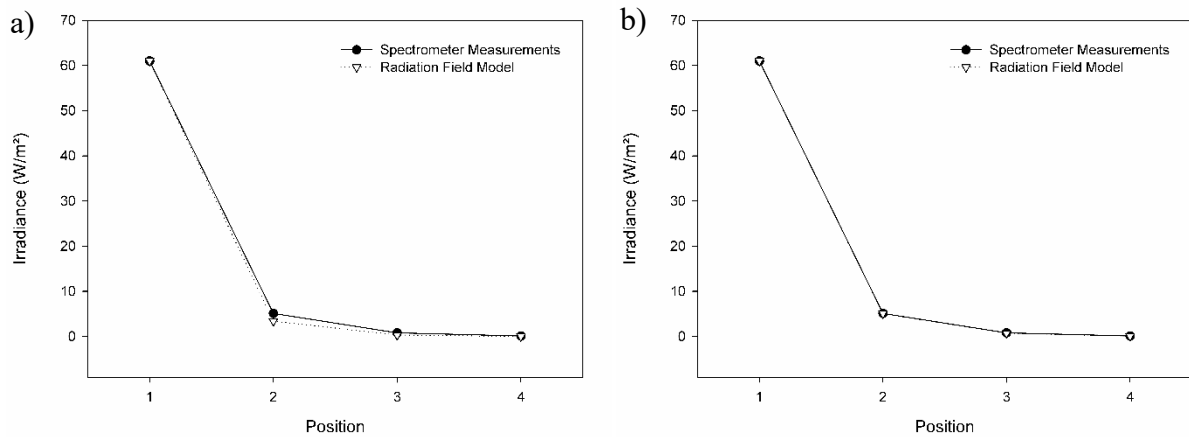
Figure 4: Irradiance predictions on the different positions for a 10 g/L P25 coating within the reactor based on spectrometer measurements, a) for initial set of parameters and b) for optimized set of parameters

1 These results were obtained for the parametric combination: $k = 0.0325$ and $\delta = 370$ nm with

2 a coefficient of determination for the log-values of 0.994. Considering the broad range of layer

3 thickness values from the literature, the optimized value of $\delta = 370$ nm is a fair approximation

4 compared to the reported value of $\delta = 450 \pm 24$ nm for a 10 g/L P25 sol-gel coating on

5 stainless steel [33]. In order to validate the optical parameters, the experiment was repeated for

6 larger parallel distances between reactor housing and lamp. The results are shown in Figure 5.

7
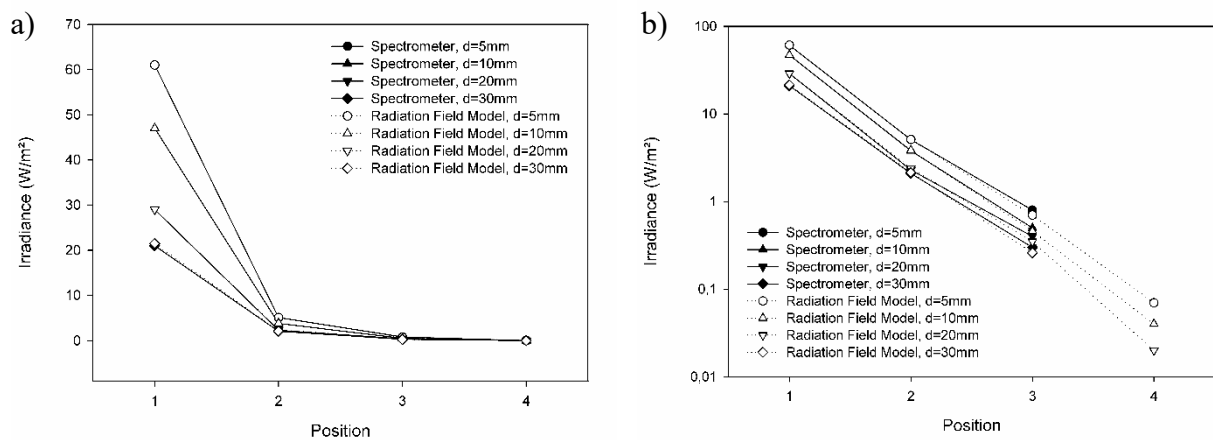
Figure 5: a) Validation of the optimized optical parameters for a 10 g/L P25 sol-gel coating by varying the distance from the UV-A lamp to the reactor housing (d=5-30mm), b) Log-scale representation to clarify the fit at low intensities

8

9 Figure 5 shows that the optical parameters can accurately predict the irradiance inside the

10 reactor for various distances of the emission source, even for low intensities as show on the log-

11 scale (Figure 5b). The intensity on position 4 is not shown in Figure 5b, since it was below the

12 detection limit of the spectrometer (<0.1 W/m²) and hence set to zero. Moreover, it can be

13 stated that the irradiance rapidly drops after passage through one coated tube with an average

14 decrease of 90% per passage.

15

16

1 The refractive index $k = 0.0325$ was assumed to be constant for the simulations of all coating

2 layers. Consequently, the layer thicknesses of the 30 g/L and 50 g/L coatings were determined

3 in a similar approach where $k = 0.0325$ was now a fixed value, resulting in $\delta = 500$ nm and

4 $\delta = 710$ nm respectively. The fitted irradiance measurements are shown in Figure 6.
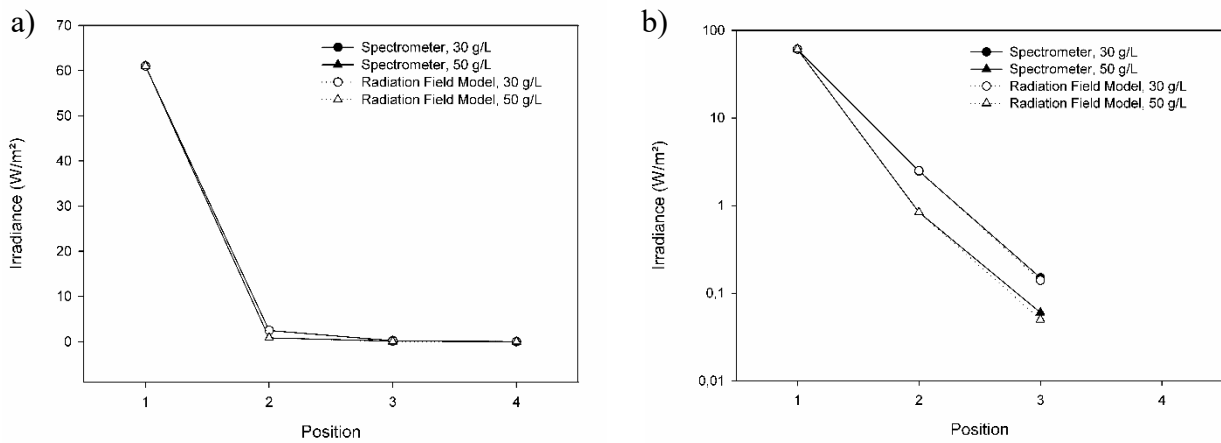

Figure 6: a) Irradiance predictions on the different positions for 30 and 50 g/L P25 coatings within the reactor based on spectrometer measurements, b) Log-scale representation to clarify the fit at low intensities (irradiance on position 4 equals zero in all cases).

5 Based on this assumption, the optical parameters were used to predict the irradiance distribution

6 inside the reactor for the photocatalytic experiments with 2 UV-A lamps. The ray trajectories,

7 departing from the two lamps, and their power are illustrated in Figure 7.

1
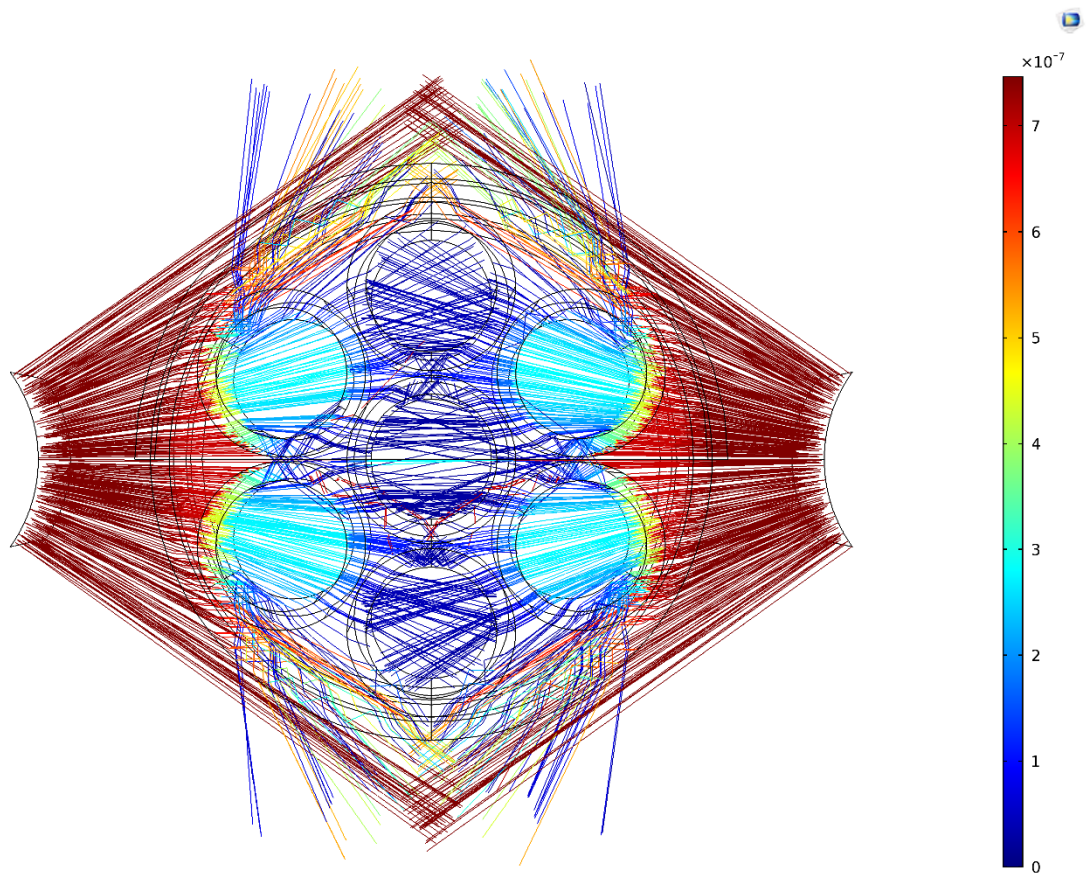
Figure 7: Power (W) of the rays, propagating through the system (climate chamber set-up, 10 g/L P25 coating), where refraction and absorption occurs.

2

3 The ray power is reduced each time it passes a coating layer and the rays are refracted at each

4 material discontinuity. Figure 7 shows the ray trajectory halfway the simulation and only a

5 fraction of the rays is shown to keep the figure clear. The computation of the ray trajectory was

6 finished when all rays reached beyond the reactor geometry. This last time step was considered

7 a steady-state solution. Consequently, the ray properties were translated into a boundary

8 condition by accumulators, resulting in an irradiance distribution on the catalytic surface (An

9 example is illustrated in Figure 8 and Video 1). Additionally, the irradiance distribution was

10 plotted against the cumulative illuminated surface area for both experimental set-ups and all

11 investigated coating layers (Figure 9). The catalytic surface receives higher irradiance for the

climate chamber set-up for all coatings, simply because the parallel distance from the emission source to the reactor housing is much smaller. Moreover, it is clear that the coating surfaces with lower P25-loadings receive more light due to a higher UV-light transmissibility. This way, the radiation field model provides valuable insights on irradiance distribution, which is difficult to measure with conventional spectrophotometry. Finally, this data can be used to optimize the reactor design towards the structuring of emission source(s), the choice of coating layer and the amount of power that is needed for complete mineralization. Based on Figure 9, the integration of emission sources within the reactor will certainly improve the uniformity of the irradiance distribution, optionally combined with an external emission source. Furthermore, higher irradiance uniformity of the multi-tube photoreactor would be achieved by varying the coating layer thickness, deposited on the tubes, as a function of their distance from the lamp.
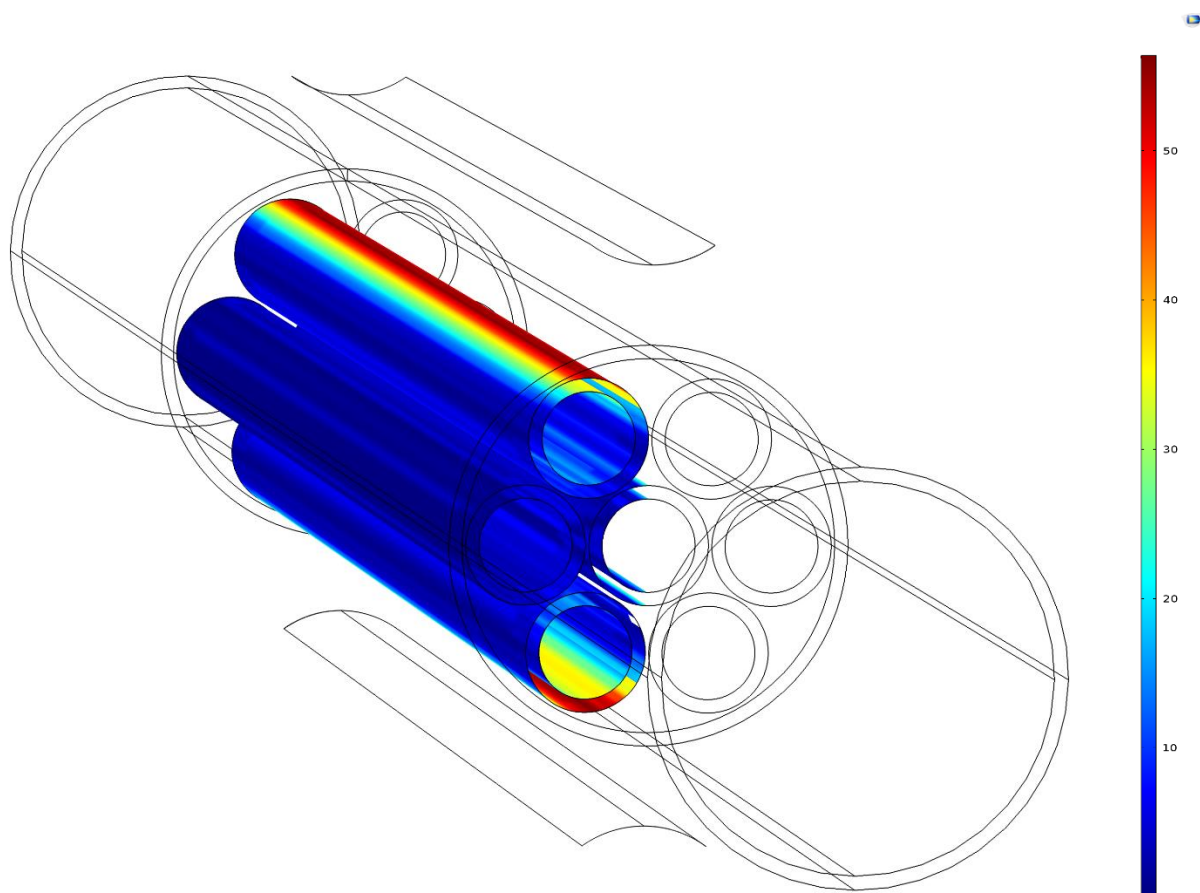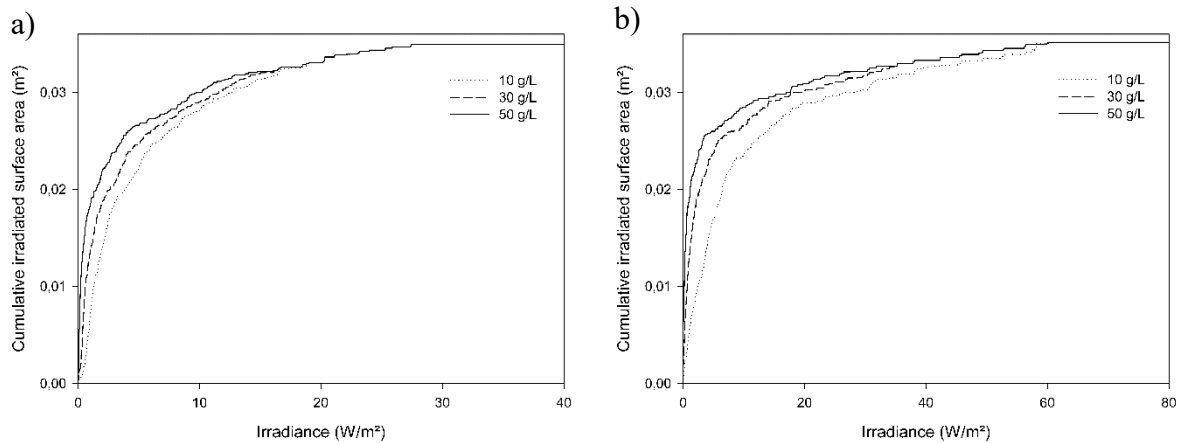

Figure 8: Example of irradiance distribution (W/m²) on the 10 g/L P25 catalytic surface with two UV-A lamps for the climate chamber set-up.

a)

b)

Figure 9: Irradiance (W/m²) plotted against the cumulative illuminated surface area for a) the FTIR set-up and b) the climate chamber set-up and for all investigated coatings.

3.2 Air flow modeling for FTIR set-up

Figure 10 shows the steady-state velocity field, simulated with a stationary solver for an inlet flow rate of 500 cm³/min. The highest velocities occurred at the in- and outlet (maximum velocity of 0.70 m/s). The velocities in the tubes never exceed 0.05 m/s corresponding to a Reynolds number of 50, emphasizing the laminar nature of the flow. Moreover, a pressure drop of only 1 Pa was observed.
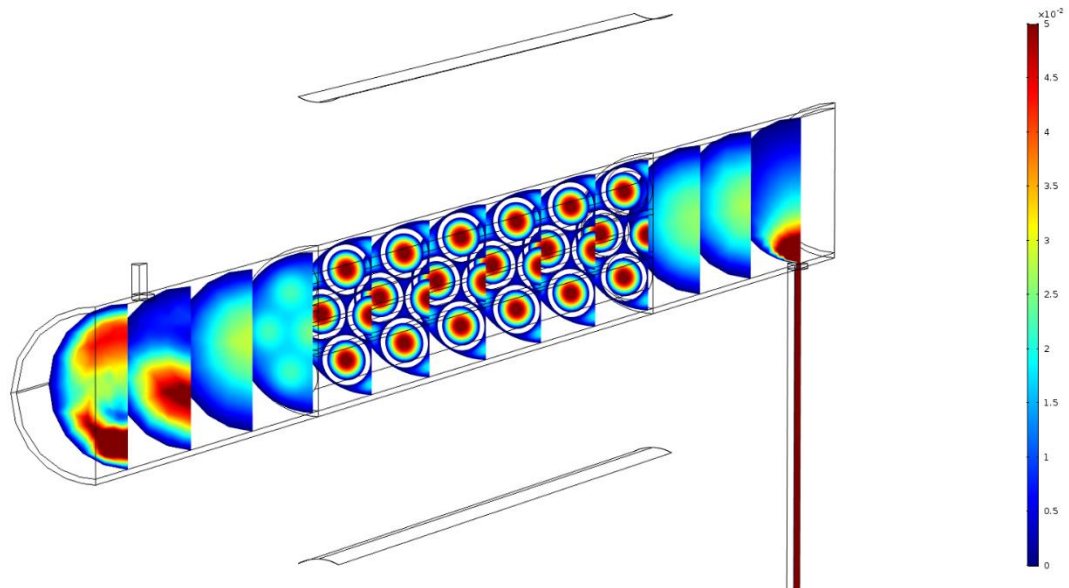
Figure 10: Velocity profile (m/s) with a flow rate of 500 cm³/min for the FTIR set-up

3.3. Intrinsic parameter estimation

The velocity field and irradiance distribution simulations allowed coupled Multiphysics modeling to predict the acetaldehyde outlet concentration. Therefore the kinetic model parameters for adsorption, desorption and photocatalytic reaction were first estimated by fitting the model results with experimental data of 4 different inlet concentrations for the 10 g/L coating simultaneously, using the Nelder-Mead optimization algorithm. Consequently, the FTIR measurements for 30 g/L and 50 g/L coatings were fitted with the same set of optimized parameters. A summary all intrinsic parameters is listed in Table 1 and the resulting fits between the Multiphysics model (using optimized intrinsic parameters) and the FTIR spectroscopy measurements are shown in Figure 11, Figure **12** and Figure **13**.

Table 1 Intrinsic parameters of the sol-gel coatings

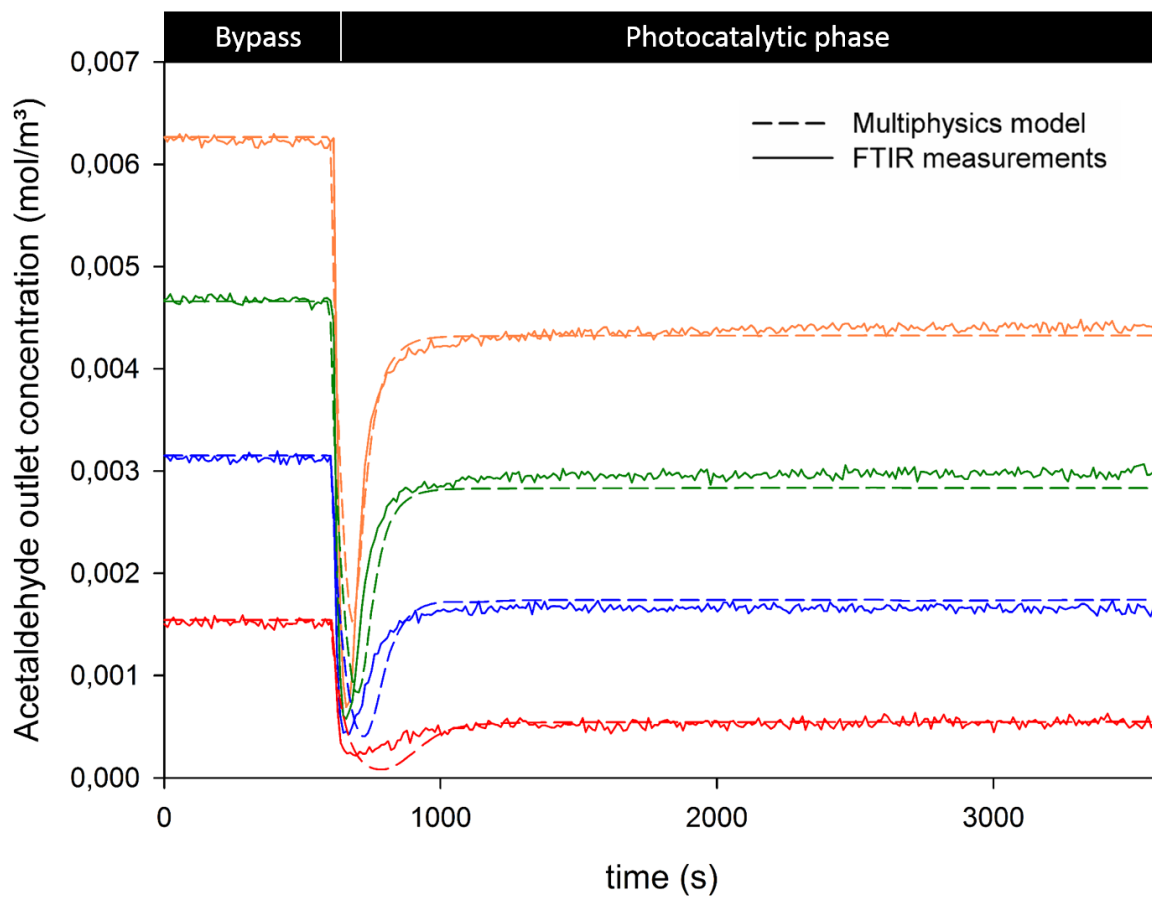| Parameter	10 g/L	30 g/L	50 g/L
k_{ads} [m/s]	2.02×10^{-3}	2.02×10^{-3}	2.02×10^{-3}
k_{des} [mol/m²s]	2.30×10^{-7}	2.30×10^{-7}	2.30×10^{-7}
k_0 [m²/W· s]	8.52×10^{-4}	8.52×10^{-4}	8.52×10^{-4}
Γ_s [mol/m²]	7.78×10^{-5}	1.28×10^{-4}	1.80×10^{-4}
δ [nm]	370	500	710

Figure 11: Optimized Multiphysics simulations based on the FTIR measurements of the 10 g/L P25 coating. The different colors (yellow, green, blue and red) each represent a different acetaldehyde inlet concentration.

1

2

3

4

5

6

7

8

9
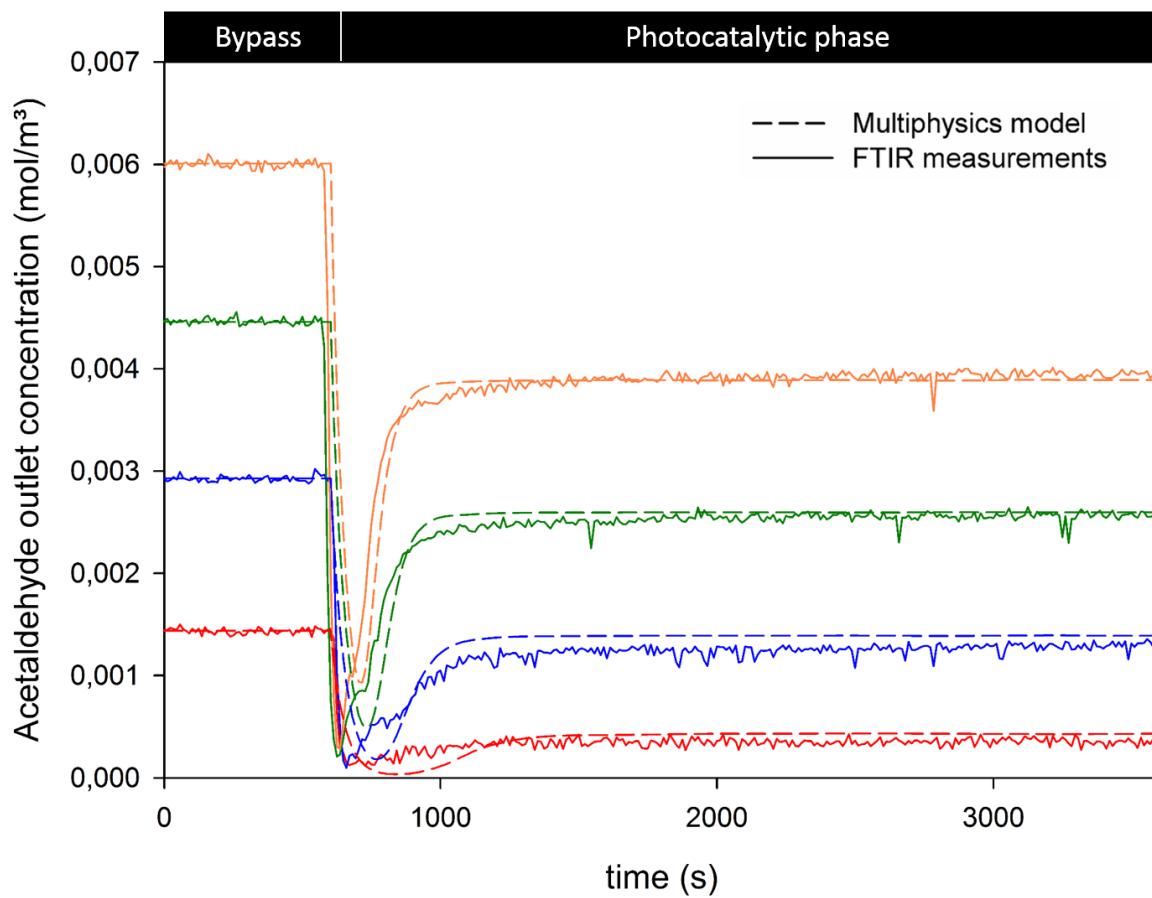
Figure 12: Optimized Multiphysics simulations based on the FTIR measurements of the 30 g/L P25 coating. The different colors (yellow, green, blue and red) each represent a different acetaldehyde inlet concentration.

1

2

3

4

5

6

7

8
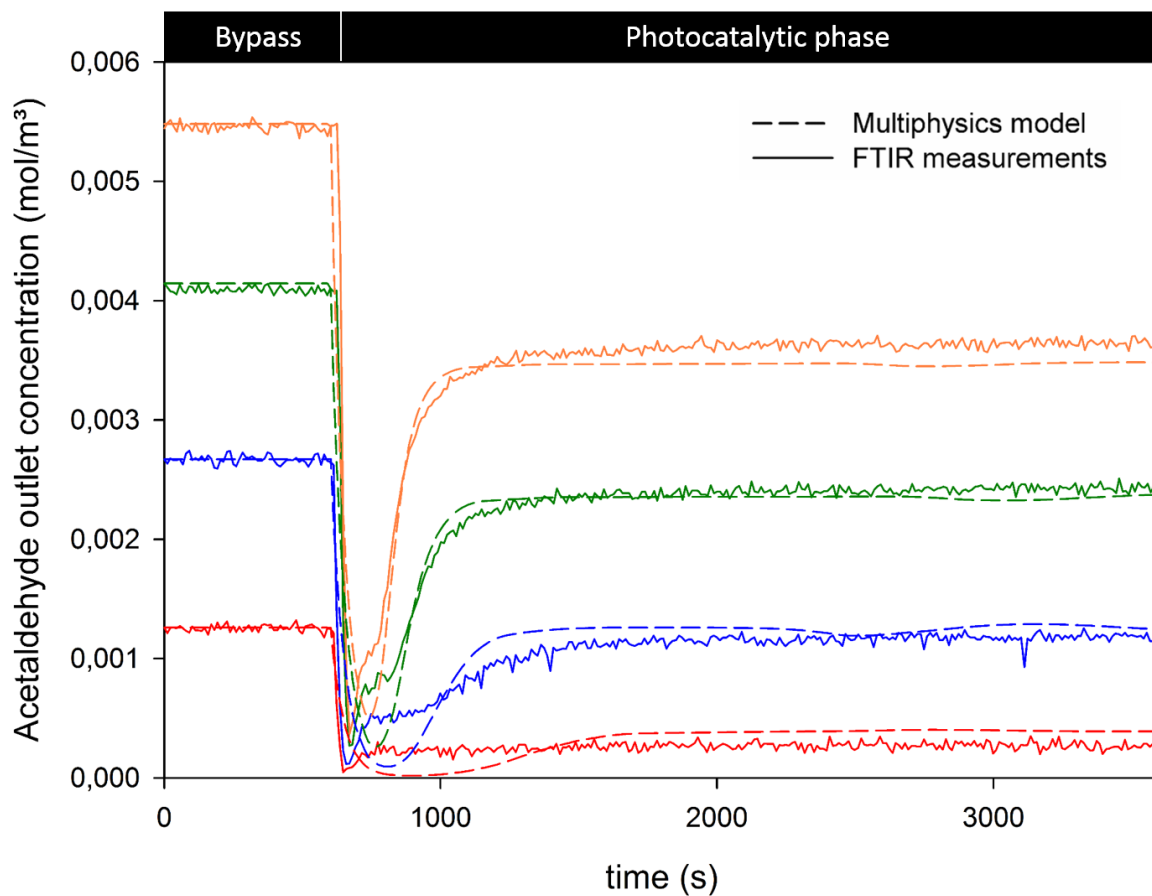
Figure 13: Optimized Multiphysics simulations based on the FTIR measurements of the 50 g/L P25 coating. The different colors (yellow, green, blue and red) each represent a different acetaldehyde inlet concentration.

1

2 The first 10 min in the figures represent the bypass phase, where the exact inlet concentration

3 is determined as an input parameter for the Multiphysics model. At the end of the bypass phase,

4 the UV-lights were activated and the air flow was switched from bypass to the reactor, hence

5 initiating the photocatalytic phase. The large drop in concentration is due to simultaneous

6 adsorption/desorption and mineralization and eventually it reaches a steady-state. The same

7 trend was observed in the simulated acetaldehyde concentrations. Although the model couldn't

8 always accurately predict the concentration (especially in the dynamic conditions right after

9 activating the UV lights), the steady-state outlet concentrations coincide well with the

10 experimental data in all cases. Therefore the prediction was successful, especially considering

the fact that all simulations were performed with the same set of intrinsic parameters for
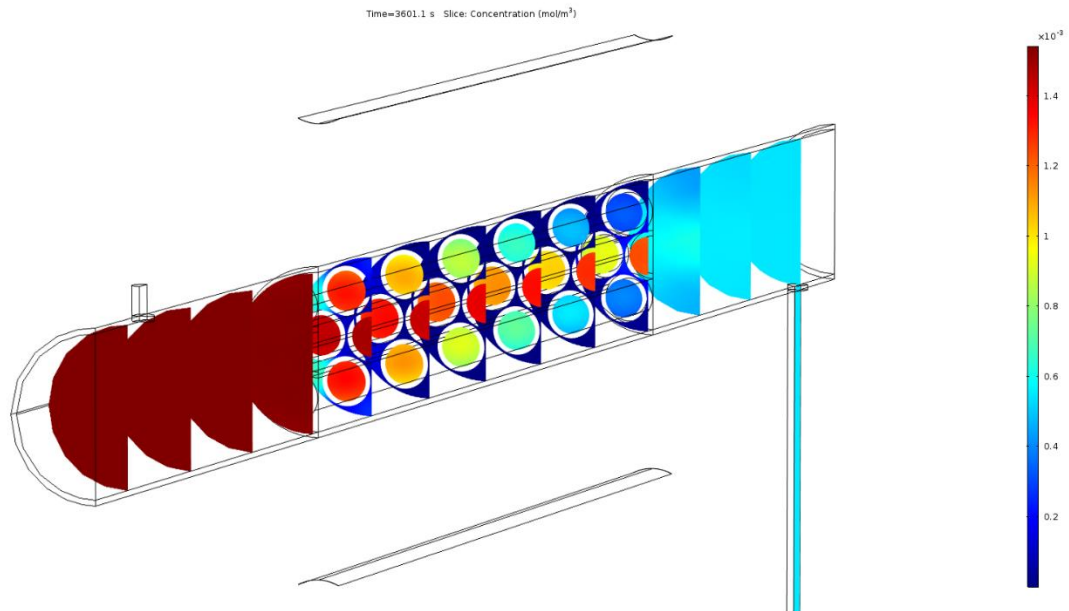adsorption, desorption and mineralization.

Figure 14: Simulated concentration profile at time step t=3600 s (steady-state) for a 10 g/L
P25 coating at an inlet concentration of 1.50×10^{-3} mol/m³

Figure 14 shows cross-section planes of the steady-state concentrations (t=3600s) within the
reactor, for a 10 g/L P25 coating at an inlet concentration of 1.50×10^{-3} mol/m³ (lowest
concentration). This figure substantiates the advantages of Multiphysics Modeling, since it
provides new insights on the concentration profile and the impact of the irradiance on the
concentration, which is very hard to measure in an experimental set-up. For example, it can be
observed that an incoming concentration of 1.50×10^{-3} mol/m³ acetaldehyde is almost
completely mineralized in the outer glass tubes, closest to the UV-light source, while the glass
tubes in the center receive much less UV-light, hence the inlet concentration is only reduced by
20%. These valuable insights can be taken into account for future optimization of the reactor
design, especially for the configuration of the emission sources.

3.4. Validation test in climate chamber

A k-ε-turbulent incompressible air flow model was used to simulate the steady-state velocity profile for the climate chamber set-up, as shown in Figure 15. The inlet velocity and the pressure drop are 1.36 m/s and 12 Pa respectively, determined by the fan characteristics. The turbulent flow is emphasized by a maximum Reynolds number of 3000 near the in- and outlet of the reactor. In the tubes a laminar flow is observed (average Reynolds number of 980).
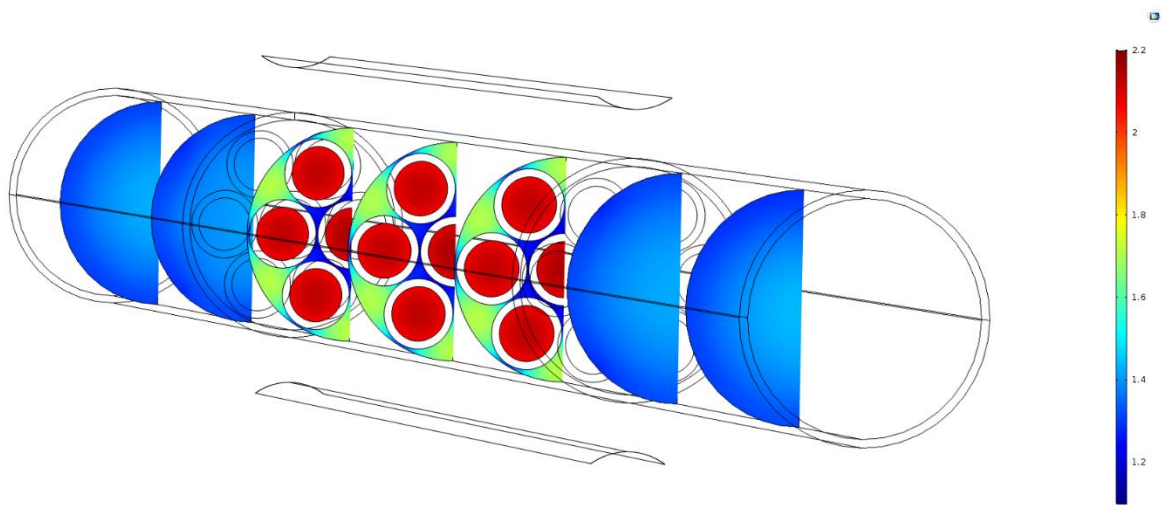
Figure 15: Velocity profile (m/s) for the climate chamber set-up

Consequently, the intrinsic parameters for each individual coating were validated against the transient acetaldehyde concentration for the climate chamber experiments. The resulting fits are shown in Figure 16, Figure 17 and Figure 18.
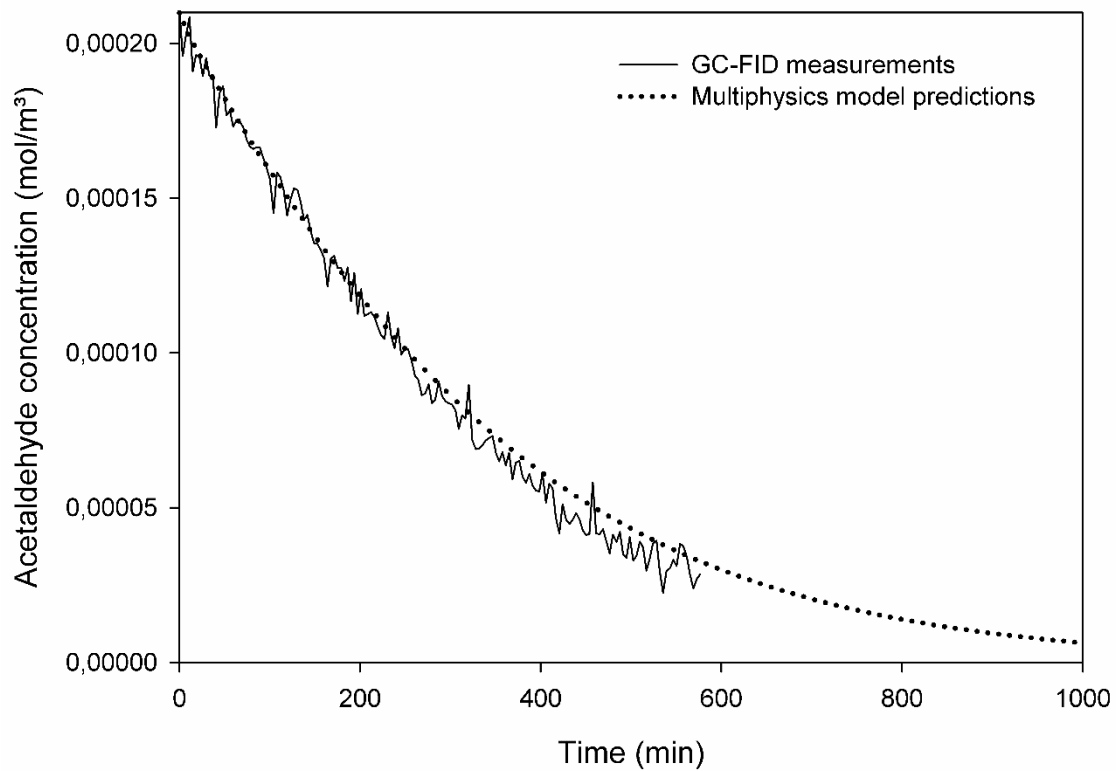
Figure 16: GC-FID measurements of acetaldehyde concentration (mol/m³) for the 10 g/L sol-gel coating and resulting fit of the Multiphysics model simulation
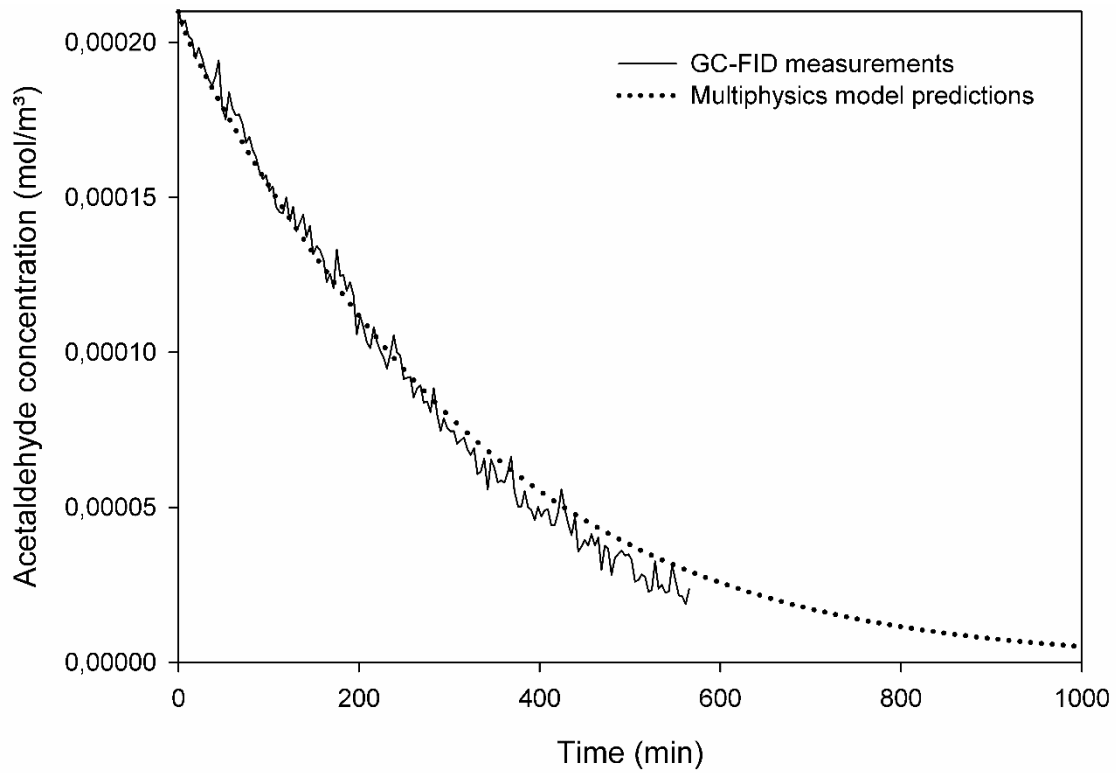
1

Figure 17: GC-FID measurements of acetaldehyde concentration (mol/m³) for the 30 g/L sol-gel coating and resulting fit of the Multiphysics model simulation
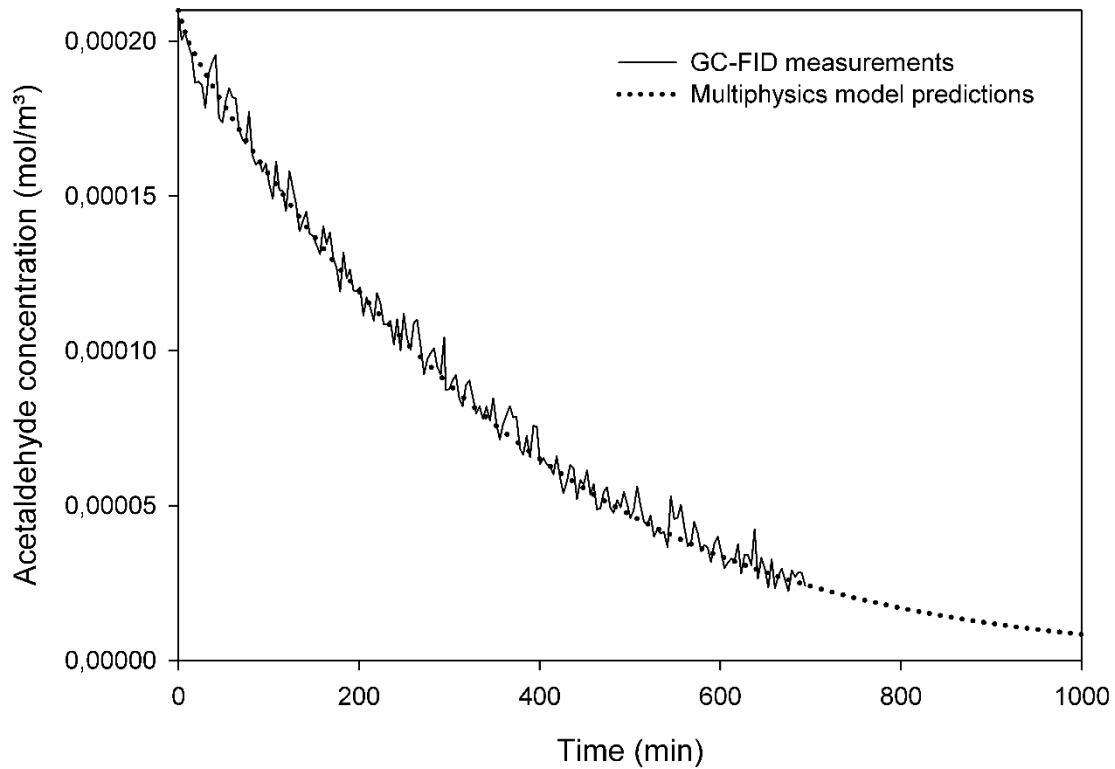
2

Figure 18: GC-FID measurements of acetaldehyde concentration (mol/m³) for the 50 g/L sol-gel coating and resulting fit of the Multiphysics model simulation

1

2   The estimated transient acetaldehyde concentrations coincide well with the GC-FID

3   measurements, as evidenced by a coefficient of determination of 0.987, 0.988 and 0.991 for 10,

4   30 and 50 g/L P25 coatings respectively. This clearly shows the independency of the intrinsic

5   parameters towards completely different operating conditions. Although the results from FTIR

6   measurements show a significant difference in degradation rate between the various sol-gel

7   coatings (van Walsem *et al.*, submitted in CES), the mineralization rate in the climate chamber

8   is very similar for all coatings. Strikingly, the Mulitphysics model was able to predict these

9   results, based on parameter optimization with the FTIR results.

10

From this ultimate valdiation test we can conclude that the modeling approach is quite reliable, given the coupling between complex physics, and that the obtained intrinsic parameters can be deployed to predict transient acetaldehyde concentrations under different conditions.

4. Conclusions

A Multiphysics model has been developed to predict concentrations of acetaldehyde in a multi-tube reactor at different operating conditions. A radiation field model was able to accurately predict the irradiance distribution in the reactor with optimized parameters for the imaginary part of refractive index and layer thickness of 10, 30 and 50 g/L sol-gel coatings, based on experimental irradiance measurements. The simulated irradiance was coupled with Computational Fluid Dynamics to predict the local photocatalytic reaction rate. The reaction rate constant was proposed be a first order relation to the UV-light irradiance up to 10 W/m² and a half order relation for higher irradiance. The reaction rate constant, adsorption rate constant and desorption rate constant were optimized, using the Nelder-Mead optimization algorithm to predict transient outlet concentrations of acetaldehyde, based on FTIR measurements. The optimized intrinsic parameters were validated for the same reactor in a climate chamber set-up, with lower acetaldehyde concentration, higher irradiance and higher air flow rates. Although a significant difference was observed in irradiation distribution, the degradation curves were more or less the same for each coating in contrast to the FTIR experiments, suggesting a mass transfer limitation in the climate chamber experiment with higher flow rates. From this validation experiment we can conclude that the developed Multiphysics model is a useful tool for performance predictions of complex photocatalytic reactor devices, such as the multi-tube reactor. The results from the batch experiment indicate the need for improvement of the current reactor design for commercial purposes. Future

development could focus on incorporating UV-lamps inside the reactor for better photon utilization. A trade-off must be made between incorporating sufficient lamps in the reactor device for efficient degradation of pollutants and a higher power consumption with an increasing number of lamps. The reactor needs a scale-up, both in diameter and length to provide adequate contact time between pollutant and catalyst. The developed Multiphysics model provides a useful and convenient tool to realize this optimization.

5. Acknowledgement

6. References

[1]   S.O. Hay, T. Obee, Z. Luo, T. Jiang, Y. Meng, J. He, S.C. Murphy, S. Suib, The viability of photocatalysis for air purification, Molecules. 20 (2015) 1319–1356. doi:10.3390/molecules20011319.

[2]   L. Zhong, F. Haghighat, Photocatalytic air cleaners and materials technologies – Abilities and limitations, Build. Environ. 91 (2015) 191–203. doi:10.1016/j.buildenv.2015.01.033.

[3]   J. Zhao, X. Yang, Photocatalytic oxidation for indoor air purification: A literature review, Build. Environ. 38 (2003) 645–654. doi:10.1016/S0360-1323(02)00212-3.

[4]   Y. Paz, Application of TiO2 photocatalysis for air treatment: Patents' overview, Appl. Catal. B Environ. 99 (2010) 448–460. doi:10.1016/j.apcatb.2010.05.011.

[5]   T. Ochiai, A. Fujishima, Photoelectrochemical properties of TiO2 photocatalyst and its applications for environmental purification, J. Photochem. Photobiol. C Photochem. Rev. 13 (2012) 247–262. doi:10.1016/j.jphotochemrev.2012.07.001.

[6]   J. Mo, Y. Zhang, Q. Xu, J.J. Lamson, R. Zhao, Photocatalytic purification of volatile organic compounds in indoor air: A literature review, Atmos. Environ. 43 (2009) 2229–2246. doi:10.1016/j.atmosenv.2009.01.034.

[7]   N. Costarramone, B. Kartheuser, C. Pecheyran, T. Pigot, S. Lacombe, Efficiency and harmfulness of air-purifying photocatalytic commercial devices: From standardized chamber tests to

nanoparticles release, Catal. Today. 252 (2015) 6–11. doi:10.1016/j.cattod.2015.01.008.

[8]   G.B. Raupp, A. Alexiadis, M.M. Hossain, R. Changrani, First-Principles Modeling, Scaling Laws and Design of Structured Photocatalytic Oxidation Reactors for Air Purification, Catal. Today. 69 (2001) 41–49. doi:10.1016/S0920-5861(01)00353-4.

[9]   M. Mohseni, F. Taghipour, Experimental and CFD analysis of photocatalytic gas phase vinyl chloride (VC) oxidation, Chem. Eng. Sci. 59 (2004) 1601–1609. doi:10.1016/j.ces.2004.01.017.

[10] A. Queffeulou, L. Geron, E. Schaer, Prediction of photocatalytic air purifier apparatus performances with a CFD approach using experimentally determined kinetic parameters, Chem. Eng. Sci. 65 (2010) 5067–5074. doi:10.1016/j.ces.2010.05.024.

[11] J. van Walsem, S.W. Verbruggen, B. Modde, S. Lenaerts, S. Denys, CFD investigation of a multi-tube photocatalytic reactor in non-steady-state conditions, Chem. Eng. J. 304 (2016) 808–816. doi:10.1016/j.cej.2016.07.028.

[12] S.W. Verbruggen, M. Keulemans, J. van Walsem, T. Tytgat, S. Lenaerts, S. Denys, CFD modeling of transient adsorption/desorption behavior in a gas phase photocatalytic fiber reactor, Chem. Eng. J. 292 (2016) 42–50. doi:10.1016/j.cej.2016.02.014.

[13] S.W. Verbruggen, S. Lenaerts, S. Denys, Analytic versus CFD approach for kinetic modeling of gas phase photocatalysis, Chem. Eng. J. 262 (2015) 1–8. doi:10.1016/j.cej.2014.09.041.

[14] F. Denny, J. Scott, V. Pareek, G. Ding Peng, R. Amal, CFD modelling for a TiO2-coated glass-bead photoreactor irradiated by optical fibres: Photocatalytic degradation of oxalic acid, Chem. Eng. Sci. 64 (2009) 1695–1706. doi:10.1016/j.ces.2008.12.021.

[15] M.E. Leblebici, J. Rongé, J.A. Martens, G.D. Stefanidis, T. Van Gerven, Computational modelling of a photocatalytic UV-LED reactor with internal mass and photon transfer consideration, Chem. Eng. J. 264 (2015) 962–970. doi:10.1016/j.cej.2014.12.013.

[16] I. Salvadó-Estivill, D.M. Hargreaves, G.L. Puma, Evaluation of the intrinsic photocatalytic oxidation kinetics of indoor air pollutants., Environ. Sci. Technol. 41 (2007) 2028–2035. doi:10.1021/es061569o.

[17] Z. Wang, J. Liu, Y. Dai, W. Dong, S. Zhang, J. Chen, CFD modeling of a UV-LED photocatalytic odor abatement process in a continuous reactor, J. Hazard. Mater. 215–216 (2012) 25–31. doi:10.1016/j.jhazmat.2012.02.021.

[18] B. Hauchecorne, D. Terrens, S. Verbruggen, J.A. Martens, H. Van Langenhove, K. Demeestere,

S. Lenaerts, Elucidating the photocatalytic degradation pathway of acetaldehyde: An FTIR in situ study under atmospheric conditions, Appl. Catal. B Environ. 106 (2011) 630–638. doi:10.1016/j.apcatb.2011.06.026.

[19]   S.W. Verbruggen, K. Masschaele, E. Moortgat, T.E. Korany, B. Hauchecorne, J.A. Martens, S. Lenaerts, Factors driving the activity of commercial titanium dioxide powders towards gas phase photocatalytic oxidation of acetaldehyde, Catal. Sci. Technol. 2 (2012) 2311. doi:10.1039/c2cy20123b.

[20]   S.W. Verbruggen, S. Deng, M. Kurttepeli, D.J. Cott, P.M. Vereecken, S. Bals, J.A. Martens, C. Detavernier, S. Lenaerts, Photocatalytic acetaldehyde oxidation in air using spacious TiO2 films prepared by atomic layer deposition on supported carbonaceous sacrificial templates, Appl. Catal. B Environ. 160–161 (2014) 204–210. doi:10.1016/j.apcatb.2014.05.029.

[21]   T. Tytgat, B. Hauchecorne, M. Smits, S.W. Verbruggen, S. Lenaerts, Concept and validation of a fully automated photocatalytic test setup., J. Lab. Autom. 17 (2012) 134–43. doi:10.1177/2211068211424554.

[22]   G.E. Imoberdorf, F. Taghipour, M. Keshmiri, M. Mohseni, Predictive radiation field modeling for fluidized bed photocatalytic reactors, Chem. Eng. Sci. 63 (2008) 4228–4238. doi:10.1016/j.ces.2008.05.022.

[23]   V. Pareek, S. Chong, M. Tad, A.A. Adesina, Light intensity distribution in heterogenous photocatalytic reactors, Asia-Pacific J. Chem. Eng. 3 (2008) 171–201. doi:10.1002/apj.129.

[24]   M. Singh, I. Salvadó-Estivill, G. Li Puma, Radiation field optimization in photocatalytic monolith reactors for air treatment, AIChE J. 53 (2007) 678–686. doi:10.1002/aic.11093.

[25]   A.L.L. Zazueta, H. Destaillats, G. Li Puma, Radiation field modeling and optimization of a compact and modular multi-plate photocatalytic reactor (MPPR) for air/water purification by Monte Carlo method, Chem. Eng. J. 217 (2013) 475–485. doi:10.1016/j.cej.2012.11.085.

[26]   COMSOL Multiphysics® v. 5.2. COMSOL AB, Ray Optics User's Guide, Stockholm, 2017.

[27]   X. Wang, G. Wu, B. Zhou, J. Shen, Optical constants of crystallized TiO2 coatings prepared by sol-gel process, Materials (Basel). 6 (2013) 2819–2830. doi:10.3390/ma6072819.

[28]   P. Chrysicopoulou, D. Davazoglou, C. Trapalis, G. Kordas, Optical properties of SiO2-TiO2 sol-gel thin films, J. Mater. Sci. 39 (2004) 2835–2839. doi:10.1023/B:JMSC.0000021461.07870.d0.

[29]   N. Negishi, K. Takeuchi, T. Ibusuki, Preparation of the TiO2 Thin Film Photocatalyst by the Dip-

Coating Process, J. Sol-Gel Sci. Technol. 13 (1998) 691–694. doi:10.1023/a:1008640905357.

[30] J. Soufi, M. Pastor-Franco, S. Zhou, R. Hardala, F. Houillon, V. Meille, D. Richard, Toward the control of thickness and uniformity in the coating of TiO2-P25 on glass, Part. Sci. Technol. 34 (2016) 229–234. doi:10.1080/02726351.2015.1068898.

[31] N. Negishi, K. Takeuchi, T. Ibusuki, Surface structure of the TiO2 thin film photocatalyst, J. Mater. Sci. 33 (1998) 5789–5794. doi:10.1023/a:1011204001482.

[32] Y. Takahashi, Y. Matsuoka, Dip-coating of TiO2 films using a sol derived from Ti (O-i- Pr) 4-diethanolamine-H20-i- PrO H system, J. Mater. Sci. 23 (1988) 2259–2266. doi:10.1007/BF01115798.

[33] K. Van Wesenbeeck, Plasma catalysis as efficient and sustainable air purification technology, University of Antwerp, 2016.

[34] COMSOL Multiphysics® v. 5.2. COMSOL AB, CFD Module User's Guide, Stockholm, 2017.

[35] P. Atkins, J. De Paula, Atkins' Physical chemistry 8th edition, Chemistry (Easton). (2009) 926–928. doi:10.1021/ed056pA260.1.

[36] R. Yang, Y.P. Zhang, R.Y. Zhao, An improved model for analyzing the performance of photocatalytic oxidation reactors in removing volatile organic compounds and its application, J. Air Waste Manage. Assoc. 54 (2004) 1516–1524.

[37] J. Peral, D.F. Ollis, Heterogeneous photocatalytic oxidation of gas-phase organics for air purification: Acetone, 1-butanol, butyraldehyde, formaldehyde, and m-xylene oxidation, J. Catal. 136 (1992) 554–565. doi:10.1016/0021-9517(92)90085-V.

[38] O.M. Alfano, M.I. Cabrera, A.E. Cassano, Photocatalytic Reactions Involving Hydroxyl Radical Attack, J. Catal. 172 (1997) 370–379. doi:10.1006/jcat.1997.1858.

[39] F. Salvadores, R.I. Minen, J. Carballada, O.M. Alfano, M.M. Ballari, Kinetic Study of Acetaldehyde Degradation Applying Visible Light Photocatalysis, Chem. Eng. Technol. 39 (2016) 166–174. doi:10.1002/ceat.201500507.

[40] COMSOL Multiphysics® v. 5.2. COMSOL AB, Optimization Module User's Guide, Stockholm, 2017.